



Inspection of Radiation Shielding Proficiency and Effect of Gamma-Ray on ESR and Thermal Characteristics of Copper Oxide Modified Borate Bioglasses

A. M. Abdelghany¹ · H. M. Diab² · A. M. Madbouly³ · F. M. Ezz-EIDin⁴

Received: 20 January 2022 / Accepted: 14 April 2022 / Published online: 10 May 2022
© The Author(s) 2022

Abstract

Samples of copper-modified bioactive borate glasses were synthesized and their radiation shielding properties including gamma-ray and neutron radiation shielding were investigated. Further, the glasses' mass attenuation coefficients were measured with a NaI(Tl) detector while their gamma-ray shielding parameters were estimated using Phy-X/PSD program. Free-radical densities were measured via electron spin resonance to estimate the absorbed doses during accidental irradiation. The extensive reduction of the dose detection threshold (2 Gy) required the estimation of the signal of the non-irradiated sample. In addition, the effects of applied microwave power and absorbed dose on synthesized samples were studied. Finally, the thermal annealing of the emerging peaks, which were due to the irradiation signal-to-noise ratio and energy dependence, was studied to estimate the stabilities of such peaks. This modified material is recommended to detect and monitor the gamma-radiation dose because of its good dosimetric properties. Finally, regarding the presence of the two borate groups, triangular and the tetrahedrally coordinated, in their definite and typical wavenumbers, the FTIR spectra displayed simplified vibrations that were close to those of many bioglasses. This paper provides complementary results for the author's previous research examining this glass for low photon dose measurements using luminescence characteristics.

Keywords Shielding parameters · ESR · Bioactive glass · CuO · Glass-dosimeter · Thermal annealing · FTIR

1 Introduction

Glassy systems are essential in many applications, including laboratory equipment, optoelectronics materials, thermal insulators, reinforcement materials, and radiation shielding materials, owing to their exceptional chemical properties, such as high densities, high refractive indexes, high infrared

(IR) transparencies, and superior gamma-ray shielding capabilities [1].

Owing to the widespread utilization of nuclear technology, the concept of nuclear radiation protection has recently attracted enormous attention. Radioactive gamma sources have also enjoyed increased utilization in different fields, including medicine, biological research, sanitization, and the industry. This type of radiation can ionize media and emit secondary charged particles via complex mechanisms. Because of the impending dangers of these radiations to people, the environment, and degradation-prone materials, it is critical to improving radiation shielding materials [2].

Some special types of glass materials were recently employed for radiation dosimetry via different physical methods [3, 4]. The monitoring of the resonance absorption of microwave power by unpaired electron spins in a magnetic field is called electron spin resonance (ESR). Different authors have explored ESR [3–5] to identify transition-metal ions that exhibit many applications. ESR dosimetry is a determining quantitative measurement of the free radicals induced by radiation in certain materials. For intermediate

✉ A. M. Madbouly
basmala1811@gmail.com

¹ Spectroscopy Department, Physics Research Institute, National Research Centre, 33 Elbehouth St., Dokki, Giza 12311, Egypt

² Ionizing Radiation Metrology laboratory, National Institute of Standards (NIS), Giza, Egypt

³ Nuclear and Radiological Safety Research Centre, Radiation Safety Department, Egyptian Atomic Energy Authority, Cairo, Egypt

⁴ National Centre for Radiation Research & Technology, Egyptian Atomic Energy Authority, Cairo, Egypt

and high-level dose standardizations, ESR dosimetry with alanine (amino acid) is employed [6]. Many researchers have studied new different materials that can be employed as ESR dosimeter materials [7, 8].

Bioglass is considered a base material for a new ESR dosimeter. The ESR dosimetry technique has been used to estimate radiation doses in the population due to many radiation accidents [9]. The lower detection limit of ESR dosimetry of tooth enamels is approximately 2 Gy [10], while the upper dose limit is > 10 kg [11]. Recent researchers have invested efforts to investigate the possibility of ESR dosimetry to lower the dose levels by chemically reducing induced ESR signals.

Borate glass is one of the famous glass-forming systems. It is considered an ideal and effective case in the IR spectroscopy of glass science. Boron, considered the smallest mass-forming element and exhibits the main vibrational signal that correlates with the glass network, arises in the mid-IR region over 500 cm^{-1} . The vibrational modes of metal-ion sites, which are active below $\sim 600\text{ cm}^{-1}$, are considered isolated from the other network styles, i.e., in the far-IR region [12], because of boron's ability to alter its arrangement with oxygen between three (BO_3) and four (BO_4). It supplies the anionic environment domain that could regulate the changeable metal ions. Therefore, the frameworks of bioactive borate glass, which exhibits a short-range, are being considered models for examining the IR region to arrange the structure of the network located at the mid-IR and the intuitive metal-ion location within the spectrum of the distant IR region. It is well-known that Cu particles are distributed within the glass network via several valence states, such as copper oxide (CuO (cuprous oxide and/or cupric oxide) and metallic copper (Cu^+) owing to its electronic shells, which $3d104s1$ represents. The color of CuO -doped phosphate glasses generally depends on the Cu^{+2} particles, which induce defect centers through the adsorption band and visible regions. These defect centers can be modified. They can be diminished or expanded after determining the radiation-causing changes in the absorbance, supporting the production of a dosimeter from inactive glass. Furthermore, Cu particles can increase the ionic quality, and the glass network's electrical and optomechanical properties, by upgrading the glass matrix's homogeneity [13]. These characters avail information for utilizing Cu^+ -doped bioglasses as a glass dosimeter for a wide range of light dosages.

However, the increasing reputation of boron in recent years [14–17], particularly in radiation shielding applications, has prompted extensive research of the optical properties and radiation attenuation capabilities of the studied glasses. These explanations have yielded the creation of an $x\text{BaO}$ ($40-x$) $\text{Li}_2\text{O}6\text{B}_2\text{O}_3$ glass system, as well as the investigation of its optical and radiation shielding

properties. It was hypothesized that barium oxide (BaO) and lithium oxide (Li_2O) substitutions would cause different behavioral changes in the optical and gamma-ray attenuation properties of the studied borate glasses. This study's findings can extend the literature on radiation shielding materials. Further, the authors believe that these findings will be beneficial to the scientific community by availing a basis for the further study of these materials regarding their mechanical and thermal properties and their durability.

The samples employed here were prepared by the same researchers in their previous work [3, 12]. However, this study aims to investigate the radiation shielding efficiency of the prepared glasses within the photon energy range of $0.015\text{--}10\text{ MeV}$, as well as the effective, fast neutron (Σ_R) removal cross-sections. Further, the ESR dosimetry technique in this study was compared with alanine dosimetry under the same conditions regarding their relative sensitivities. Furthermore, the sensitivities of the prepared samples compared with the alanine reference dosimeter in the gamma dose range of the intermediate-range were tested. Concurrently, a different technique other than ESR spectroscopy, i.e., Fourier-transform IR (FTIR), was achieved for radiation dose reconstruction.

2 Experimental Work

2.1 Substances Preparations

The glass samples, a member of the Hensch bioglass family with a nominal composition of $45\text{B}_2\text{O}_3\text{--}24.5\text{Na}_2\text{O--}24.5\text{CaO--}6\text{P}_2\text{O}_5$, and other samples with the same compositions in which the CuO content attained (4 g/100 g batch) added overweight in in the expense of all other components and gradual increase to retrace the effect both lower and higher addition. Studied samples were synthesized via the traditional melt annealing routine. The glass samples were prepared with chemically pure H_3BO_3 , CaCO_3 , Na_2CO_3 , and $\text{NH}_4\text{H}_2\text{PO}_4$ that Raysan Chemicals supplied, as presented in Table 1 Further, calculated quantities of the prepared material were weighed before the material was melted in a Pt–2% Rh ceramic container in a Vecstar induction melting furnace for 3 h at $1100\text{ }^\circ\text{C}$. The melts were rotated periodically to obtain homogeneous, glassy materials. Thereafter, the glass melt was cast into preheated molds exhibiting the required dimensions. The prepared glass samples were transferred immediately into the muffle furnace exhibiting an annealing temperature of $380\text{ }^\circ\text{C}$. After annealing for 1 h at a heating rate of $25\text{ }^\circ\text{C h}$, the annealing muffle was allowed to cool slowly to room temperature.

Table 1 Chemical compositions (wt%) and density for glass samples

Sample	B ₂ O ₃	Na ₂ O	CaO	P ₂ O ₅	CuO /100 g batch	Density (gm/cm ³)
BGCu0.0	45.0	24.50	24.50	6.0	0.0	2.62
BGCu0.2	44.95	24.45	24.45	5.95	0.2	2.64
BGCu1.0	44.75	24.25	24.25	5.75	1.0	2.69
BGCu2.0	44.5	24.00	24.00	5.5	2.0	2.75
BGCu4.0	44.0	23.50	23.50	5.0	4.0	2.88

2.2 Gamma-Ray Shielding Properties

The experimental linear attenuation coefficients (LAC) are determined by utilizing a gamma-ray spectrometer system which consists of NaI (TI) Scintillation detector (Oxford model) with 3" × 3", amplifier and 16 k multi-channel analyzer.

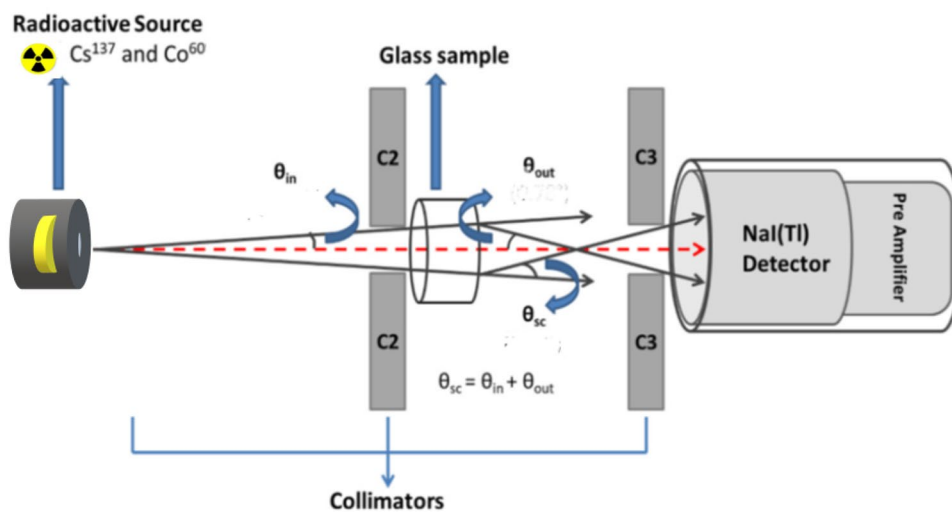
The attenuation of the glass sample was measured using narrow beam gamma-ray transmission geometry. The source was housed in a lead container with a 0.5 cm face aperture. Each glass sample was placed on a specimen holder 5 cm away from the source. The distance between the source and the detector was kept constant at 10 cm. The detector was properly shielded with lead to prevent scattered radiations from nearby objects from reaching the detector. The sum of the incidence beam divergence (θ_{in}) and the angle subtended by exit collimation (θ_{out}) is the total scatter acceptance angle (θ_{sc}). For the present geometry, the incidence beam divergence was 1.63°, the acceptance angle at the detector was 0.72° and scatter acceptance angle was 2.6°, where Fig. 1 depicts the geometry experimental setup of the gamma-ray spectrometer system. [18, 19].

The detector was covered by lead bricks and kept away from the room's walls to protect it from secondary radiations (background, bremsstrahlung, and fluorescence).

Genie2000 software was used to record and analyse the spectra. To keep the statistical error below 1%, the detector's actual time was set to 600 s for each measurement. The background counts were recorded for the same amount of time (600 s) and utilized to adjust the measurements. The experimental LAC value has been determined as the arithmetic mean of the five experimentally observed LAC-values.

The LAC (cm⁻¹) of all glass samples are calculated for gamma-rays of energies 662, 1173, and 1333 keV from radioactive point sources (where their activity is 5 μ Ci) ¹³⁷Cs and ⁶⁰Co, respectively. LAC can be evaluated by utilizing Brew Lambert's law equation [19], the mass attenuation coefficients MAC (cm²/g) are calculated for samples, by dividing LAC by the density (ρ) of the glasses samples (g/cm³) [20]. Half value layer (HVL), Mean free path (MFP), effective atomic number (Z_{eff}), effective electron density N_{eff} , radiation protection efficiency (RPE%), electrical conductivity C_{eff} , effective removal cross-sections for fast neutrons (Σ_R), and energy absorption build-up factor have been estimated by Phy-X/PSD software. It is recommended to look at the reference [21, 22] with an explicit routine interpretation of all relevant equations. After that, for a description of the Phy-X/PSD software used [23].

Fig. 1 The geometry experimental setup of the gamma-ray spectrometer system



2.3 Gamma-Irradiation Regime

The samples were exposed in batches to different gamma-irradiation doses from a Cs-137 at the Laboratory of Ionizing Radiation Metrology, Egyptian National Institute of Standards (NIS). The irradiation of the batches was performed at a dose rate of 23 rad/min. Where, the dose rate from radioactive source was calculated by multiplying specific gamma ray constant (Γ) due to photons with energy (E) by activity of radioactive source (A) at a time (t) and divided it by square the distance (d) by using the equation ($D = \frac{\Gamma A t}{d^2}$) [24]

The calculated weight of the powdered bioactive borate glass sample was 100 mg and that of the standard alanine pellet was 65 mg. The temperature and pressure of the samples were recorded before and after the irradiation by calibrated thermometer and parameter. The values from the readings of the absorbed dose were calculated employing an NPL electrometer exhibiting an ionization chamber (NE-2561) calibrated at the Bureau International Des Poids Et Mesures (BIPM), France, with a combined uncertainty of 0.30%. The calibration of the doses was indicated by air kerma (K_{air}) at the International Atomic energy Agency, following a code of practice guide [25].

2.4 Characterization

An X-band ESR spectrometer (Bruker, EMX) was employed for the measurements by applying the standard rectangular cavity (4102ST) under operational conditions of 9.7 GHz and a modulation frequency of 100 kHz. Briefly, 110 mg of the borate glass samples were placed in a quartz tube (3 mm i.d.). The height of the powdered sample inside the tube was 9–10 mm, ensuring an identical cavity magnetic field. The microwave power was pre-selected to increase the “dosimetric signal point/natural signal point” ratio, while the “dosimetric signal point /low-frequency noise point” ratio decreased; thus, the microwave powers were 8, 25, and 50 mW for alanine and the bioactive glass, and the modulation amplitude was 4 G for the bioactive glass. The center of the magnetic field sweeps was 3450 G, the sweep of the magnetic field was 4000 G, the field sweep rate was 100 G/82 s, and the time constant value was 20 ms. The scans

of the field sweep were 10 and 30 in the intermediate-dose range. The receiver gain was 10^4 , and the spectrum resolution was 1024. In order to calibrate the ESR intensity, the stability of the spectrometer besides the signal g-factor was used, and the MgO was impregnated separately with the Mn standard sample. An FTIR absorption spectrometer, such as the Bruker VERTEX 70 FTIR Spectrometers, was employed to measure the IR absorption spectra at room temperature in the 4000–400 cm^{-1} range.

3 Results and Discussion

3.1 Radiation Shielding Parameters

The LAC values of the studied samples at photon energies of 662, 1173, and 1333 (KeV) were measured on a gamma-ray spectrometer system and also determined theoretical via Phys-X/PSD software at the same photon energies as listed in Table 2.

LAC is essential for evaluating glass materials' gamma-radiation attenuation shielding efficiencies. BGCu-4.0 exhibited the highest LAC value; however, as the energy increased, the LAC value decreased. Very small deviations, obtained in the LAC values obtained via experimental and theoretical methods, were typically caused by the small variations in the mathematical and physical models, the geometry, the atomic ambiguity, among other factors, for each method. Regarding all the glasses, the relative difference between the experimental method and Phys-X/PSD increased from ~0.49 to 2.01, which means there is good agreement between the two methods.

The PhysX/PSD software was used to calculate the radiation shielding parameters of the prepared glasses. Figure 2 depicts the MAC results for study samples at photon energies ranging from 0.015 to 15 MeV. Figure 2 shows that increasing the concentration of Cu increases the MAC while increasing photon energy decreases it because the interaction mechanisms of photons with matter differ depending on photon energies. With increasing photon energy, the probability of the photoelectric effect (PE) decreases, with the advantage of medium-energy Compton scattering (CS). The cross-section decreases as photon energy increases, the

Table 2 The experimental LAC (cm^{-1}) for bioactive borate glasses doped with copper oxide at different energies

Sample	662 keV			1173 keV			1333 keV		
	Exp	Theo	RD%	Exp	Theo	RD%	Exp	Theo	RD%
BGCu0	0.197	0.199	1.02	0.149	0.152	2.01	0.141	0.142	0.71
BGCu0.2	0.200	0.201	0.50	0.151	0.153	1.32	0.142	0.143	0.70
BGCu1.0	0.205	0.206	0.49	0.155	0.157	1.29	0.145	0.147	1.38
BGCu2.0	0.210	0.213	1.43	0.160	0.162	1.25	0.150	0.152	1.33
BGCu4.0	0.225	0.227	0.89	0.171	0.172	0.58	0.160	0.162	1.25

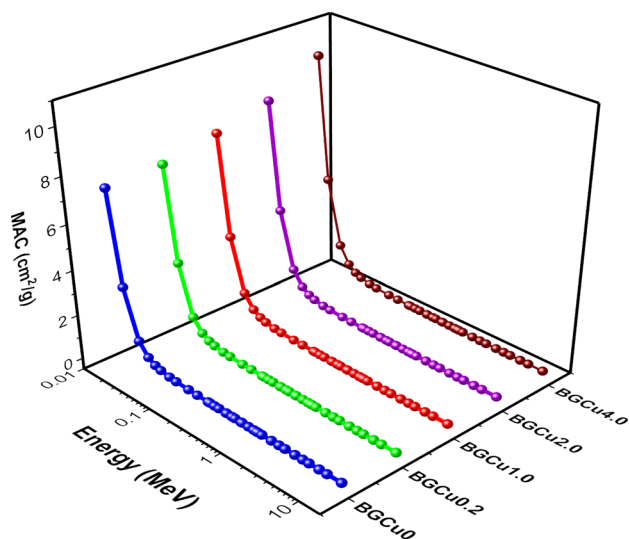


Fig. 2 The variation of MAC for studied glasses at different gamma-ray energies

pair production process (PP) displays evident dominance in the upper energy domain (beyond 12 MeV), with the cross-section varying as $\sigma_{PP} \propto \log E$ [18, 25].

Due to the high concentration of Cu, the sample BGCU4.0 has the highest values of MAC at all energies when compared to the other studied glass samples at the same energy, where attenuation is dependent on the concentration, density of the elements in the matrix, and energy of the incident photons.

HVL can provide powerful insight into the shielding competencies of a sample as it reduces the number of photons in half by setting the desired thickness, thus providing a clear indication of the sample's shielding competencies. Figure 3 shows the HVL for the glasses. It can be seen that the

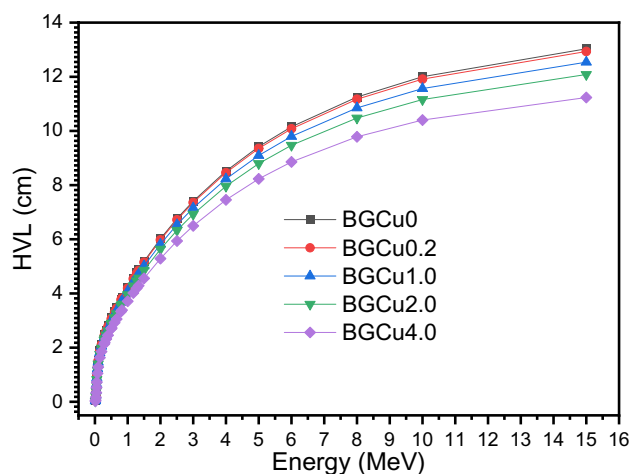


Fig. 3 The variation of HVL with energy for all studied glasses

HVL decreases as the CuO content increases. The BGCU4.0 sample with the highest concentration and density of CuO exhibited the highest absorbance of all samples tested. These results show that BGCU4.0 has the highest shielding efficiency against gamma rays as it has a higher MAC than other glasses studied. Here, the HVL value of BGCU4 is approximately 13% lower compared to the BGCU0 sample at 662 keV. Another important factor is the MFP, which accounts for the barrier's ability to reduce gamma rays. Thus, the glass with the lowest MFP shields well. The results show that as photon energy increases, so does the MFP of the glass (Fig. 4). This means that a large number of photons can pass through the glass at higher energies. It can also be seen that as the CuO content increases, the MFP value decreases significantly, which represents the average distance between two successive interactions of incident gamma photons. MFP value for studied BGCU4 glass appears to be small. Typically, because of the highest mass fraction of Cu in the tested glass than the other glasses samples.

A very relevant parameter, RPE%, was calculated for all the glasses employing the experimental results and plotted as a function of the increase in the photon energy (Fig. 5). The RPE% values varied from 18% (for unfilled BGCU-0.0) and increased with the increasing Cu concentration from 18.2% (BGCU-0.2) to 21% (BGCU4) at 662 keV. Additionally, the values of RPE% increased by ~2% for BGCU-4.0 than BGCU-0.0 at 1173 and 1333 keV. RPE% decreased with the increasing energy for all tested energies [26].

This decreasing behaviour was because higher-energy photons easily penetrated the sample, thus reducing the number of photons attenuated by the glass shield and the RPE%. These results also indicated that the BGCU-4.0 glass was more effective against lower-energy photons. Finally, the BGCU-4.0 sample exhibited the highest CuO content, making this glass the best choice for radiation shielding.

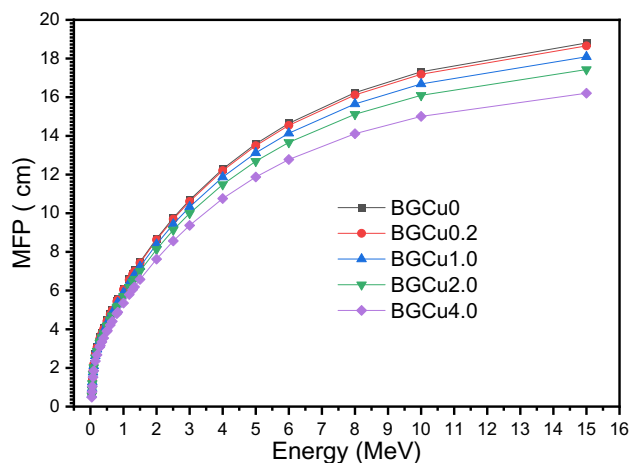


Fig. 4 The variation of MFP with energy for all studied glasses

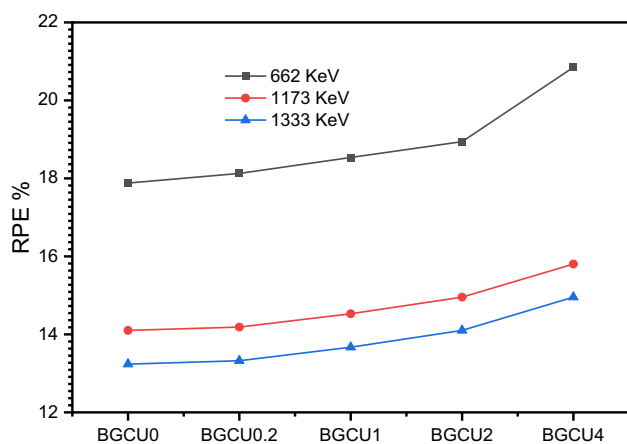


Fig. 5 The radiation protection efficiency (RPE %) for studied glasses at different gamma-ray energies

Z_{eff} is another essential factor that facilitates the determination of the attenuation capability of glass. Numerous studies have revealed that glass materials with high Z_{eff} values demonstrate excellent radiation-protection potentials [27, 28]. Figure 6 shows the Z_{eff} values of all the studied glasses in the 0.015–15 MeV photon energy range. Clearly, Z_{eff} was affected by the photon energy and the changes in the chemical composition (e.g., the addition of CuO) [27]. For all the glasses, larger values were observed in the lowest energy regions where the photoelectric effect predominates. In contrast, minimal values were observed in the medium-energy range due to the Compton scattering command and minor increments at higher energies due to the pair-production phenomenon's influence. As shown in Fig. 6, the BGCu-0.0 glass (without CuO) exhibited the lowest Z_{eff} values, while the BGCu-4.0 glass (with 4 mol% CuO) exhibited the

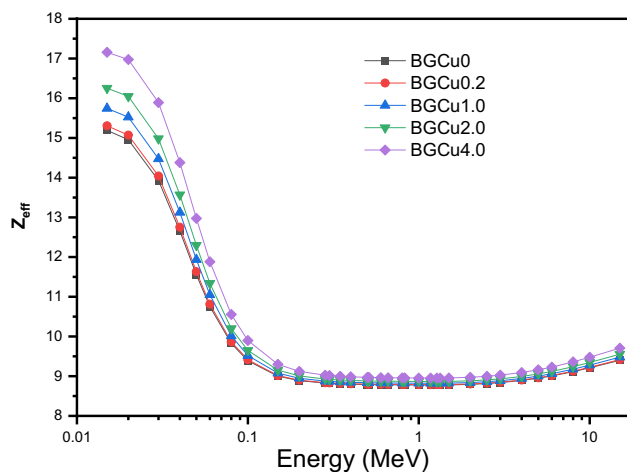


Fig. 6 Variation of effective atomic number Z_{eff} with energy for all samples with different concentrations of Cu

highest Z_{eff} values in the given photon energy range. Thus, the addition of CuO significantly increased the Z_{eff} value.

When a photon collides with an electron on glass material, it becomes a free electron. Moreover, a change in the number of free electrons would cause a change in the material's electrical conductivity. Glasses with varying conductivities based on their photon density and energy can change their shielding properties. Notably, the highest effective conductivity values were observed in the low-energy region because of the dominant photoelectric absorption there. The change in the effective conductivity was smaller in the high-energy region because the Compton scattering and pair-production processes dominated. Consequently, it is crucial to understand the C_{eff} coefficient, which demonstrates how glass retains its properties depending on the nuclear application. The N_{eff} and C_{eff} behaviours are identical to those of Z_{eff} , as illustrated in Figs. 7 and 8. Figure 9 shows the relationship between Z_{eff} , N_{eff} , and C_{eff} .

During the practical application of the prepared glass, particularly in radiation shielding, it is valuable to compare the protective properties of the prepared glass with those of some standard shields. Table 3 presents a typical comparison of the most crucial shielding parameters, including HVL, MFP, Z_{eff} , and RPE%, of BGCu-4.0 and some shielding materials. The results demonstrated that the composite in this study exhibited a high shielding efficiency, which distinguished it from the other considered shielding materials.

The absorption build-up factors are commonly used to describe gamma photon accumulation. The energy absorption build-up factor (EABF) indicates the number of photons accumulated within the thickness of the glass under consideration. The change in EABF with a photon energy range of 0.015–15 MeV, up to 40 mfp, is depicted in

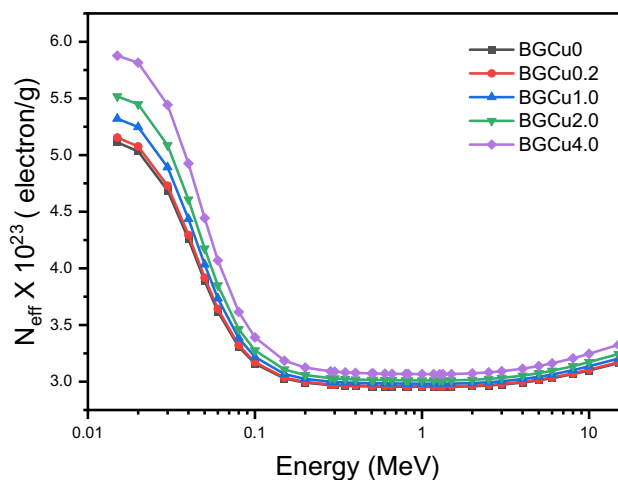


Fig. 7 Variation of effective electron density N_{eff} with energy for all samples with different concentrations of Cu

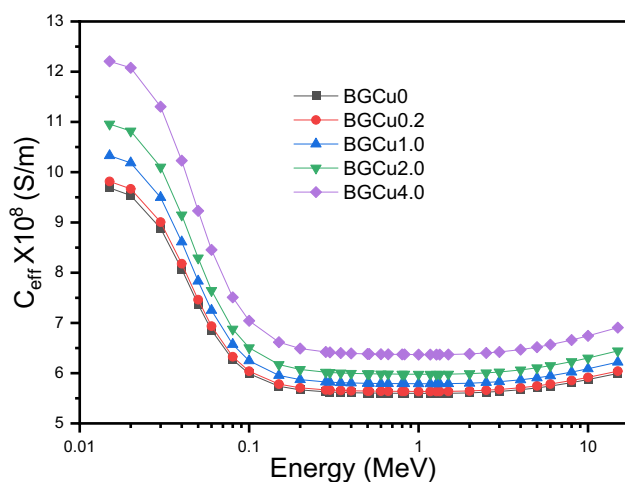


Fig. 8 Variation of effective conductivity C_{eff} with energy for all samples with different concentrations of Cu

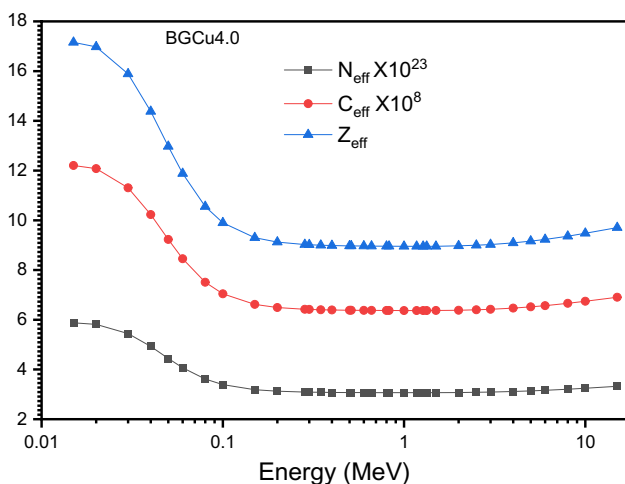


Fig. 9 Relation between Z_{eff} , N_{eff} and C_{eff} with energy for BGCu4.0 sample

Table 3 Comparison of many shielding parameters for the currently tested BGCu4 sample and various samples at 662 keV gamma energy

Samples	HVL	MFP	MAC	Z_{eff}	References
BGCu4	3.10	4.40	0.0788	8.96	This work
Hematite-serpentine	3.05	10.12	0.0787	9.98	[29]
PVC-H30	3.42	4.93	0.0795	-	[30]
Granite	3.586	5.17	0.0738	10.02	[31]
Ba polymer concrete	4.89	8.49	0.0720	10.16	[32]

Fig. 10a–d for all glasses studied, and the dynamics of the EABF coefficient with energy is the same for all glasses. The dependence of EABF values on three parameters is shown in Fig. 10 the energy of the incoming gamma photon, the

sample penetration depth in mfp, and the glass composition [19]. EABF was low at energies below 100 keV, gradually increasing up to 200 keV, then decreasing with increasing energy. First, when the photoelectric interaction almost completely eliminates the incident gamma photon, the calculated EABF values are lower. Following that, the number of photons heading up gradually increases as the interaction of Compton scattering increases. During the interaction, Compton scattering removes only a small fraction of the incident photon energy. Scattered photons, along with the rest of the incident photon energy, accumulated inside the investigated glass thickness. It's rewritten to be: "At photon energies, 1.022, pair production in the field of nuclei is the dominating absorption mechanism of photons, where 1.022 MeV is the threshold energy for electron–positron pair production". As a result, the number of EABF values gradually decreased as the incident gamma photons increased.

Second, the calculated EABF values were observed to increase systematically with increasing penetration depth up to 40 mfp. Gamma photons take longer to penetrate the thicker layer, so more photons are accumulated. It is observed that the lowest EABF values are achieved at low penetration depths (1 mfp) while the highest EABF values are obtained at large penetration depths (40 mfp). The calculated EABF values decreased with increasing CuO content, while the minimum and maximum EABFs were obtained for 3.85 and 0 wt% CuO. As the proportion of CuO content increased, the calculated EABF values increased. Therefore, the BGCu4.0 sample obtained the highest value with higher Z_{eff} values, suggesting that it is an excellent shield for gamma rays.

It is widely known that neutrons have a greater radiobiological effect than photons, which require appropriate attenuators for the safety of radiation workers [33]. In practice, neutron protection is achieved through scattering and absorption processes. For all glasses studied in Fig. 11 shows the values of Σ_R . Obviously, Σ_R values increase with increasing CuO concentration, indicating that Cu is effective Σ_R . Table 4 shows that the BGCu4.0 sample had higher Σ_R values compared to the other nuclear shielding agents.

3.2 Electron Spin Resonance Spectra

Figure 12a–c shows a standard comparison of the ESR line spectra of selected Cu-doped samples (a) before irradiation and (b) after being doped with CuO before the irradiation and after different gamma-irradiation doses (2 and 200 Gy). The irradiated samples revealed a Gaussian-shaped ESR spectrum of the unirradiated sample at $g = 2.0055$. It is evident from Fig. 12b that the ESR spectrum of the 2 Gy-irradiated samples exhibited two signals, namely the radiation-sensitive and radiation-insensitive signals. Figure 12b and c show the ESR spectra of the

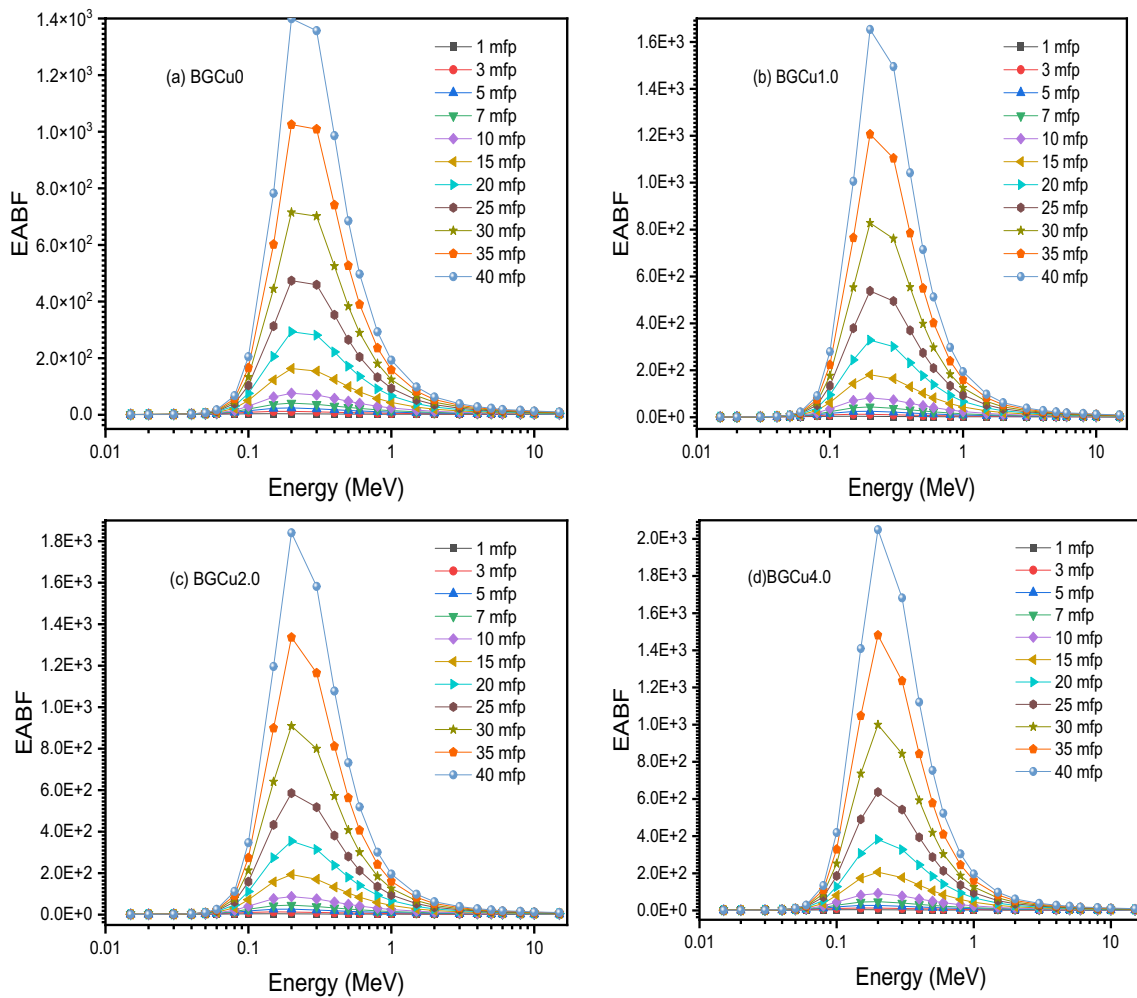


Fig. 10 a–d Variations of energy absorption build-up factor (EABF) with photon energy at different mean free paths for all glasses

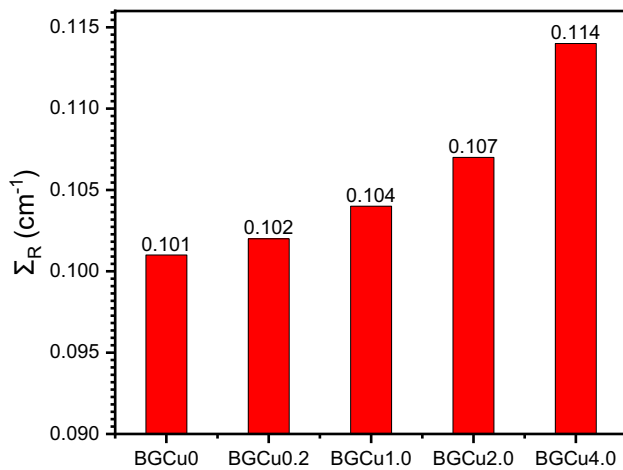


Fig. 11 Effective removal cross-sections for fast neutrons (Σ_R), for all glasses

Table 4 Comparison of Σ_R of glass BGCu4.0 with reported different nuclear radiation shielding substances

Sample	Σ_R	Reference
BGCu4.0	0.114	This work
Fluorophosphates glass S5	0.105	[22]
H ₂ O	0.1024	[34]
TBBT30 glass	0.1169	[22]
Ordinary concrete	0.0937	[29]
Hematite-serpentine concrete	0.0967	[29]
Ilmenite-limonite concrete	0.0950	[29]
Ilmenite concrete	0.1121	[29]

a sample comprising the anisotropic single sharp peak with values of $g = 1.9979$ and 2.0021 (maximum and minimum values of the signal at $g = 2.0037$ and 1.9979 , respectively). The signal corresponds to CuO [14–16]. Figure 12 shows the ESR spectra of the unirradiated and

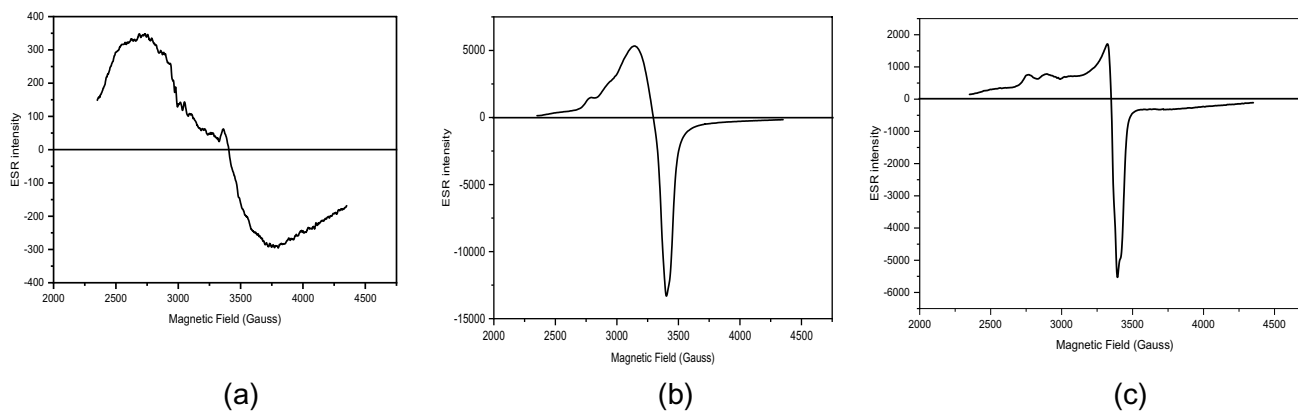


Fig. 12 Typical ESR spectra of **a** parent glass, **b** selected copper doped sample before irradiation process and **c** after being irradiated with 200 Gy ^{137}Cs gamma ray. The sweep width of magnetic field was 40 Gy

irradiated samples at 2 and 200 Gy, respectively, with a magnetic field of 4000 G. This is considered a dosimetry signal; it exhibits a linearity property with the gamma-ray dose–response, i.e., the increase in the dose linearly increased the isotropic signal line.

It has been well established that adding a copper ion in a (BGCu-0.0) glass network would benefit the prospect of investigating the topical order via ESR spectroscopy [17]. Cu^+ and Cu^{2+} are the two soluble ionic states of Cu in glasses. At room temperature, Cu^{2+} is the only cause of ESR absorptions. Cu ions in the Cu^{2+} state are of the 3d9 type, with 2D as the ground state, electron spin (S) of 1/2, and nuclear spin (I) of 3/2 for both ^{63}Cu (natural abundance, 69%) and ^{65}Cu (natural abundance, 31%) [35]. Although Cu ions are not visible during ESR absorption, they can interact with Cu^{2+} . The increase in the dislocation of the glasses structure, dipole–dipole interactions, and interactions between ions in multivalent states all contribute to the expansion at $g = 1.977$. Thus, the presence of Cu^{2+} – Cu^+ pairs and dipole–dipole interactions demonstrate the evolution of the ESR absorption line ($g = 2.01$) with the CuO material in the studied glasses. The g -factors and hyperfine constant values indicated that the bonding between Cu^{2+} and the ligand atoms was generally ionic [19], although there was a notable covalence consequence. Since Cu^{2+} is a network modifier, it competes with the borate network to form the cations for the oxygen pairs in their vicinity. Since the B–O bonds in the cumulative system involving them are weakened, the covalence bonding between Cu^{2+} and O would increase. Generally, the signal amplitude is proportional to the number of ESR active centers that are involved in resonance absorption. Thus, the drop in the line amplitude of the $g = 2.1$ resonance at 40 Gy indicated that the concentration of Cu^{2+} reduced the occurrence of diamagnetic Cu^+ , which coexists with

Cu^{2+} in the glass network when the glass is subjected to irradiation 40 Gy.

3.2.1 Microwave Power Dependence

Figure 13 indicates the dosimetric signal behavior of the samples irradiated to 200 Gy by Gamma rays (1 scan) based on the microwave power dependency. As shown by the Fig. 13, microwave power increased corresponded to a similar increase in signal intensity, which further increased exponentially before reaching saturation. A sufficiently high microwave power extending from 25 to 50 mW was optimal for these signal measurements.

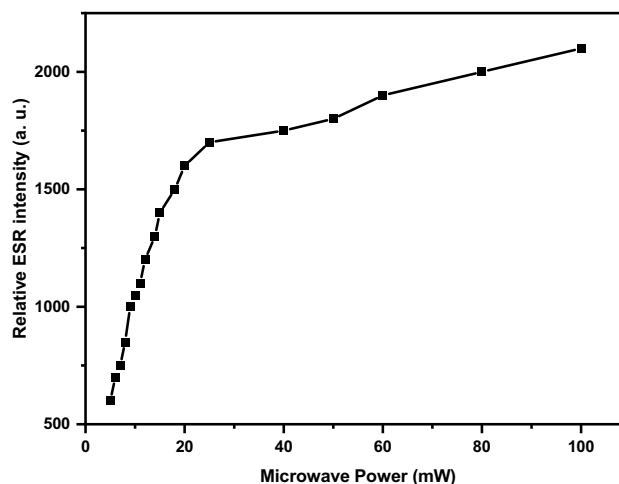


Fig. 13 200 Gy Gamma rays irradiated dosimetric signal (1 scan) based on Microwave power dependency

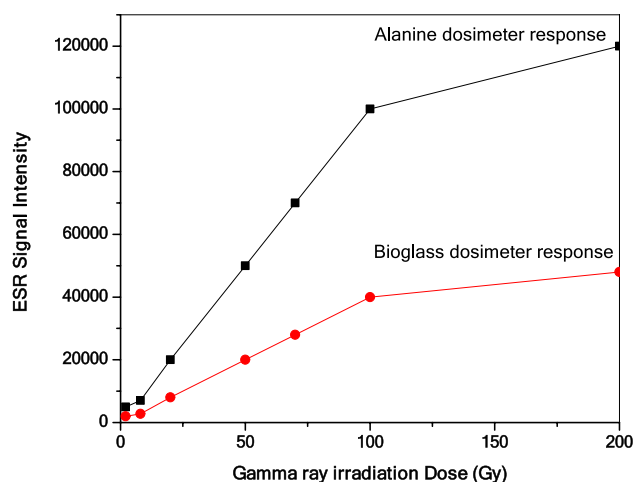


Fig. 14 Dose–response relationship for samples and alanine as a function of the dose from Cs-137 source (10 scans)

3.2.2 Dose–Response for Gamma-Ray

The relation between the different irradiation doses and the corresponding responses of the ESR signal intensities of bioglasses and alanine samples is shown in Fig. 14, showing that the CuO-doped bioglass sample exhibited excellent sensitivity, which was ~2.6 times higher than those of alanine dosimeters. In the case of intermediate-dose range (2–200 Gy), a linear relationship appeared between the bioactive borate glass-absorbed dose samples and the first derivative line of the ESR peak-to-peak height.

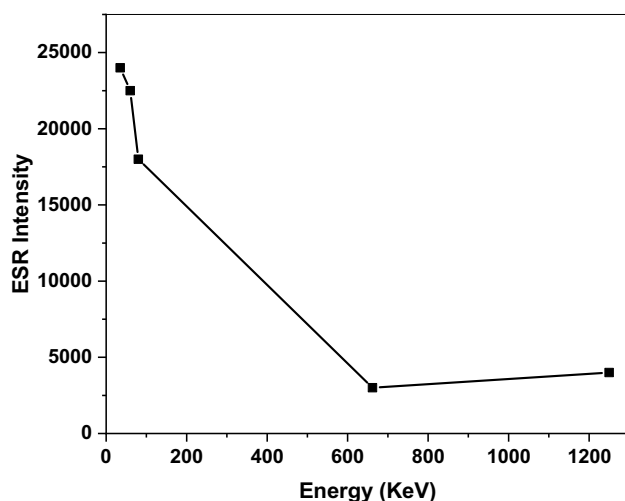


Fig. 15 Energy dependent of ESR intensity of borate bioactive glass

3.2.3 The Energy Dependency

The energy dependence of the bioactive borate glass was studied by irradiating the different samples with the same dose (2 Gy) of different radiation energies. The ESR intensities at lower energies (35, 60, and 80 keV of X-ray) were higher than those at higher energies (^{137}Cs and ^{60}Co) (Fig. 15). Additionally, the photoelectric effect controlled the dose deposition from photon energy of < 100 keV; in the case of higher energy, it was controlled by the Compton effect [36]. When alanine was irradiated, the stable free radicals, which might be measured directly, were evaluated [37].

3.2.4 Signal to Noise Ratio

Figure 16 shows that the S/N ratio of the modified borate glass was approximately 2.9 times higher than that of the alanine reference dosimeter under the same conditions, indicating the enhancement of the radiation sensitivity by the modified borate glass. This might be attributable to introducing Cu^{2+} in the glassy borate matrix that exhibited an enhanced radiation response.

3.3 Thermal Properties Stability

3.3.1 Isochronal Annealing Type

Figure 17 shows the temperature range for the isochronal annealing of the samples (25 °C–200 °C) and the related relative intensity (n/n_0) of the dosimetric signal corresponding to a certain temperature. The Figure 17 indicated that the dosimetric signal was thermally stable at different annealing temperatures, thus reflecting the availability of this material for use in detecting and monitoring radiation dose.

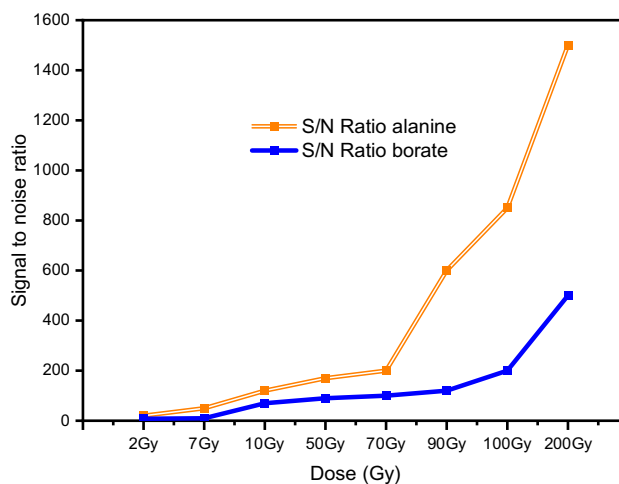


Fig. 16 Signal to noise ratio for alanine and borate bioactive glass

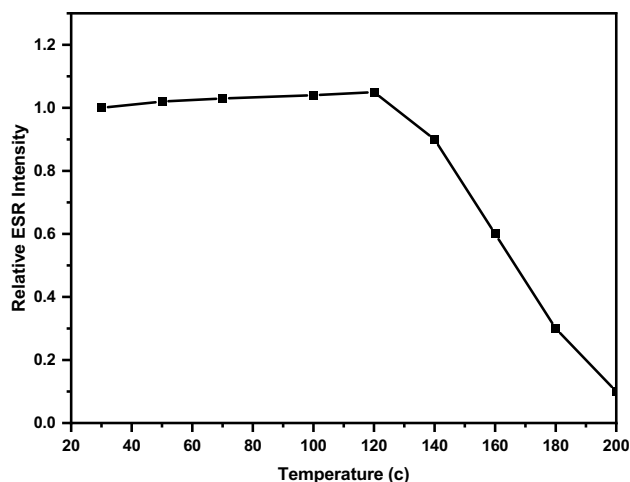


Fig. 17 Isochronal annealing of samples which is ranging from 25 up to 200 °C certain temperature and the relative intensity(n/n_0) of the dosimetric signal corresponding to a certain temperature

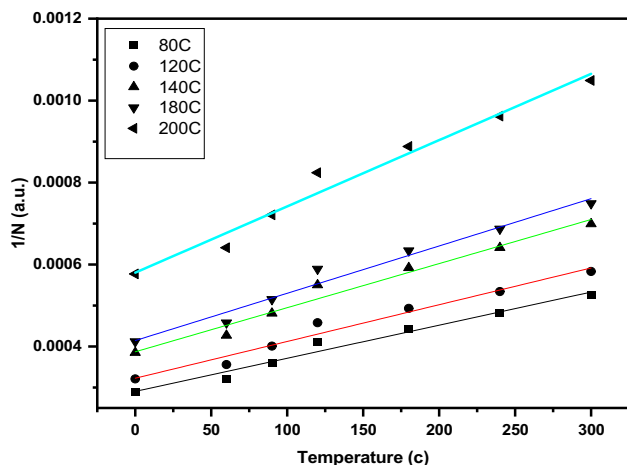


Fig. 18 Isothermal annealing study of borate bioactive glass based on time dependency and to second order decay ($1/n$)

3.3.2 Isothermal Annealing

Figure 18 shows the borate glass samples that were heated at different temperatures in a closed ESR tube. It shows the variations in the reciprocal intensity ($1/n$) after annealing as a function of the isothermal annealing time. Regarding the second-order decay, the results were plotted logarithmically. From the linear fitting slope, the lifetime of each annealing temperature of the glass sample could be evaluated.

Figure 18 shows the isothermal annealing of borate glass as a function of time, obeying the second-order decay ($1/n$).

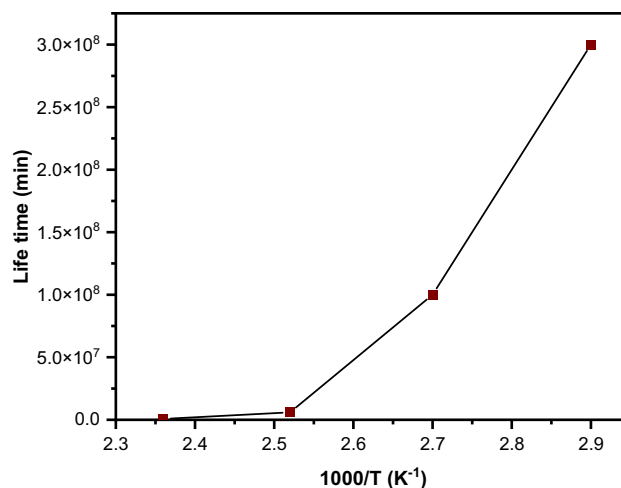


Fig. 19 Shows isothermal annealing in borate bioglasses and from Lifetimes versus ($1000/T$) which represent the reciprocal temperature experiments. At room temperature, the estimation of the straight line gives the lifetime

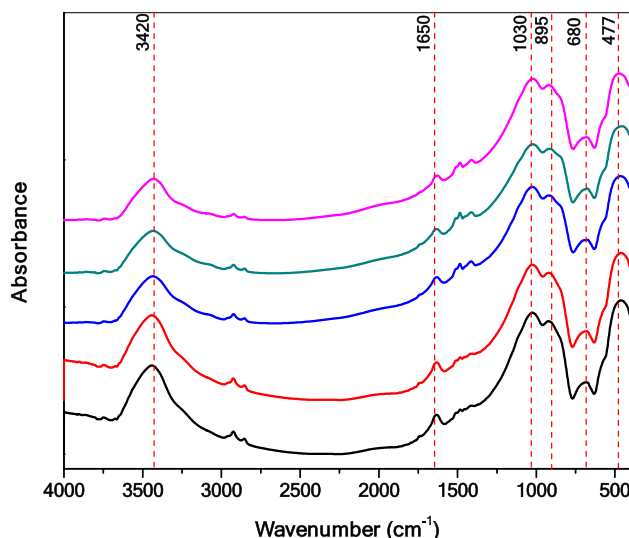


Fig. 20 FTIR absorbance of the investigated glass after irradiation

3.3.3 Activation Energy E and lifetime τ calculation

Figure 19 shows the reciprocal of Temperature ($1000/T$) versus τ formula is called Arrhenius plot in semi-logarithmic scale for borate bioglasses, activation energy calculation achieved by the equation ($E=0.1958 \times \text{slope}$) to be (19.58) eV. At 25 °C the estimation of linear fitting of the r value versus the reciprocal temperature ($1000/T$) of the Arrhenius plot in a semi-logarithmic scale was utilized to calculate the lifetime T and equal to 7×10^6 years

3.4 FTIR Measurements

3.4.1 FTIR Absorption Spectra of Glass Material Before Irradiation

The FTIR absorption spectra of the studied glassy samples containing different concentrations of Cu ions were studied, and the wavenumber spectra versus absorbance were plotted (Figure 20). The main absorption bands, which correlated with the BO_3 and BO_4 structural units, were observed and assigned. The soda-lime- B_2O_3 glass exhibited the characteristic IR spectra of combined triangular- and tetrahedral-type borate groups comprising the following spectral features:

1. Small broadband at 470 cm^{-1} usually combines with a kink near 530 cm^{-1} .
2. A rounded peak with low intensity at 680 cm^{-1} .
3. A broad middle curved band at 895 cm^{-1} .
4. A broad strong band at 1030 cm^{-1} .
5. A small peak at 1650 cm^{-1} .

Borate glasses are fascinating solid materials because of their rich chemistry, as well as their capability of borate to easily vary its harmonic configuration with oxygen between three (BO_3) and four (BO_4) to form a changeable structural unit in some borate glasses [38]. Additionally, the results might be due to the small mass of boron atoms compared to those of other elements, such as Si, P, or Ge.

Furthermore, the appearance of the main IR vibrational modes related to the glass network was well above 500 cm^{-1} [39], clearly distinguishing them from those of the metal-ion sites, which are active in the far-IR region. Another IR study [40] of different borate glasses with a wide range of variable compositions was recorded via the KBr disk method.

The observed IR data were compatible with those of another reference IR spectral absorption measurement employing reflectance or transmission techniques [41]. The borate glass family, which originated from boron oxide (B_2O_3), was synthesized by Zachariasen in 1932 [42] and is considered a glass former. Krogh-Moe [12] opined that borate glasses could be mainly formed from boron-oxygen triangles [BO_3], thus forming borax groups (B_3O_6).

The observed parallelism between the IR spectra of the studied samples was due to some limitations regarding the vibrational bands, as follows:

- i. A new band appeared in the middle region between 1400 and 1500 cm^{-1} with increasing intensities after doping with different Cu concentrations.
- ii. The change feature of the near IR broadband intensity settled at 895 – 1030 cm^{-1} .

- iii. Some changes in the relative area of the main mid-two broad bands extended from 800 to 1200 cm^{-1} and 1250 to 1600 cm^{-1} .
- iv. The maintenance of the vibrational band around 3420 cm^{-1} was attributed to the water or OH vibrational groups even with the change in the copper content of the glassy matrix.

3.4.2 FTIR Absorption Spectra After Irradiation

It is accepted that [43] pure borate glass is created basically of BO_3 as three-membered rings. When transition metal oxide (such as CuO) is added to borate glass, BO_3 triangles units transform to BO_4 tetrahedral units, breaking bridging oxygen bonds to shape NBOs and populate the tetrahedral network interstitial sites of the locality of non-bridging oxygens which has a negative charge. Figure 10 proves no change in band positions with increasing CuO concentrations which confirmed both BO_3 and BO_4 structural unit formation. Such spectral data (Fig. 21) indicate that there is no evidence for absorption band related to CuO, simply it has affected the stability and shares of boron in many forming units. FT-IR represents the appearance of other forming units in the glass under investigation. The known FTIR absorption bands for different B_2O_3 at ~ 720 , ~ 1260 , and $\sim 1420\text{ cm}^{-1}$, are concern the vibrations of B–O bonds in BO_3 units [43].

According to the vibrational modes of the borate glass matrix, it was divided into three infrared spectral ranges from 400 up to 4000 cm^{-1} . The location of the first group was found around 500 cm^{-1} throughout the region. These bands are due to the vibration of sodium cations in their oxygen sites [44], besides three characteristic bands for crystalline

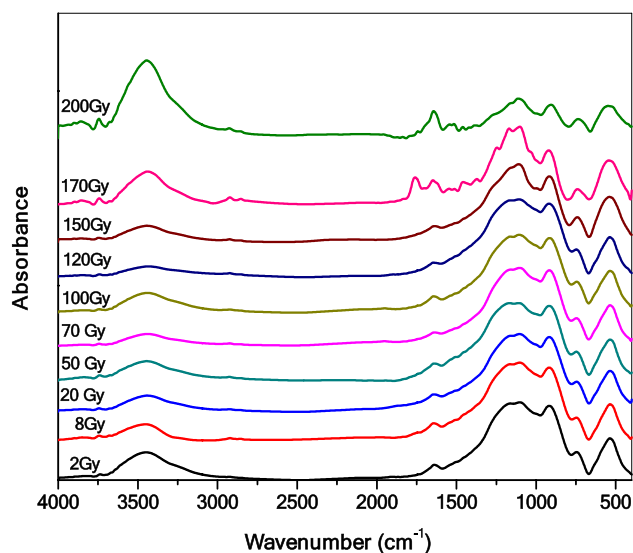


Fig. 21 FTIR absorbance of the investigated glass after irradiation

CuO were detected around ~ 410 , ~ 500 , and ~ 610 cm^{-1} , respectively, and where Cu_2O was recognized around 615 cm^{-1} . The second group of the spectrum is located in the region between 500 and 1450 cm^{-1} including the following bands 517 , 694 , 774 , 929 , 1014 , 1100 , 1240 , 1320 , and 1400 cm^{-1} . These values are in accord with the analogous observation available in the literature [45], they are happened due to the vibrational style of the borate grid. The band noticed at 517 cm^{-1} is due to some deformation mode within the glass network, whereas the band noticed at 680 cm^{-1} is related to the oxygen bridging two trigonal boron atoms (B–O–B) linkage in the borate matrix. The bands observed at 929 , 1014 and 1100 cm^{-1} are assuming B–O bond stretching of the tetrahedral BO_4 units.

Further, the bands in the spectral range of 1200 – 1400 cm^{-1} were produced by the asymmetric stretching vibration of the B–O bond of the trigonal BO_3 units in the various borate groups, such as the boroxol ring, diborane, metaborate, pyroborate, and orthoborate groups [46]. Furthermore, the existence of these bands confirmed the amorphicity of the investigated glass samples. The spectrum ranged of 1500 – 4000 cm^{-1} revealed the third group, which included several bands in part between 1500 – 1750 , 2250 – 3000 , and 3000 – 4000 cm^{-1} ; these bands might be due to the hygroscopic character of the powdered glass samples [47]. The absorption bands in the region of 3000 – 3750 cm^{-1} confirmed the existence of H_2O and the OH groups within the glass network, which resulted in the formation of bridging bonds, such as B–H–B and H–O–H. These bridging bonds generated the vibrational bands in the IR region of 1500 – 1750 cm^{-1} . Furthermore, the bands at 2338 and 2370 cm^{-1} indicated the formation of a BH_2 compound, which generally induces doublet bands, within the glass matrix. Finally, the bands at 2748 , 2854 , and

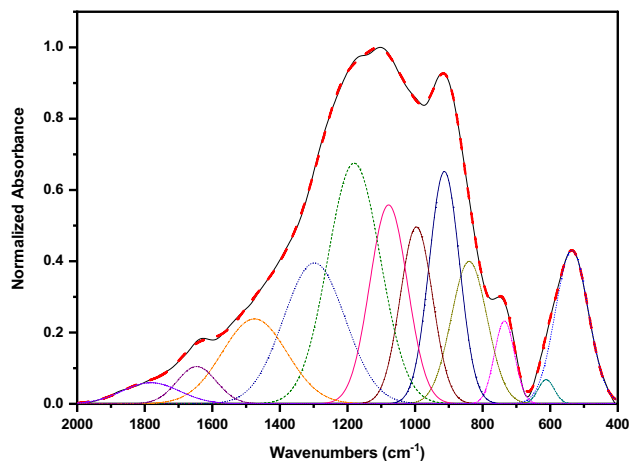


Fig. 22 Deconvolution of FTIR absorbance peaks of the investigated glass before irradiation

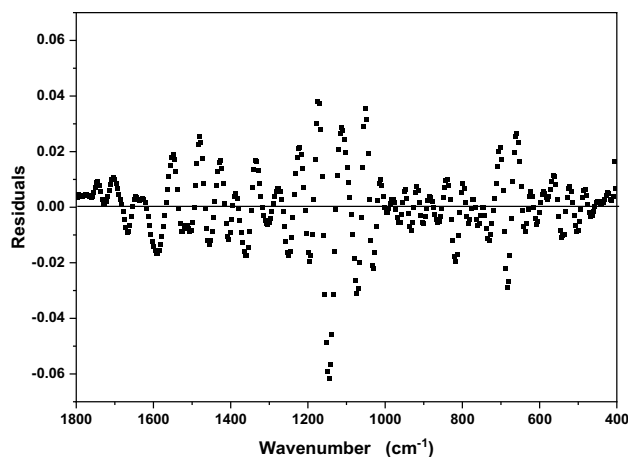


Fig. 23 An exemplified deconvolution analysis of sample that contain 1% Copper oxide before irradiation

2934 cm^{-1} might be due to the vibrations of the hydrogen bonds [48].

Comparing the FTIR spectra of the BGCu-2.0 glass after its exposure to different irradiation doses (Fig. 22) and before irradiation (Fig. 23) revealed that the IR spectra of the irradiated glass exhibited consistent vibrational absorption bands around the same locations of the unirradiated glasses. Several researchers have demonstrated that subjecting glasses to high ionizing radiation, such as gamma and X-rays, would cause several fluctuations in their chemical and physical properties [49]. Gamma rays produced the absorption bands in several spectral ranges because of the formation of defect centres due to the capture of loose electron pairs and positive holes generated by gamma-irradiation operations. Furthermore, some authors concluded that shielding occurs as the transition metals oxide-doped glasses are exposed to consecutive gamma-irradiation doses

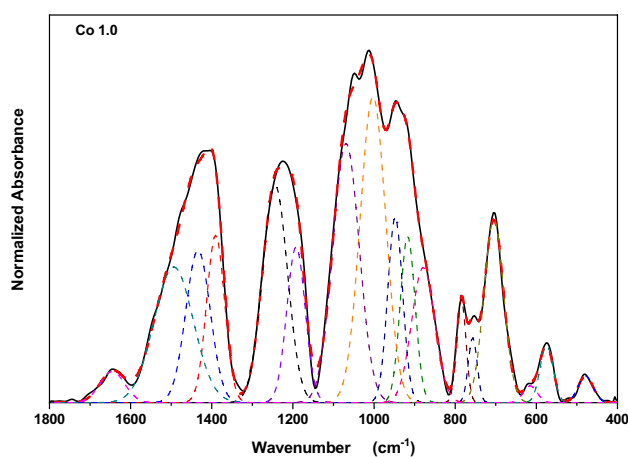


Fig. 24 Deconvolution of FTIR absorbance peaks of the sample containing 1% CuO after irradiation

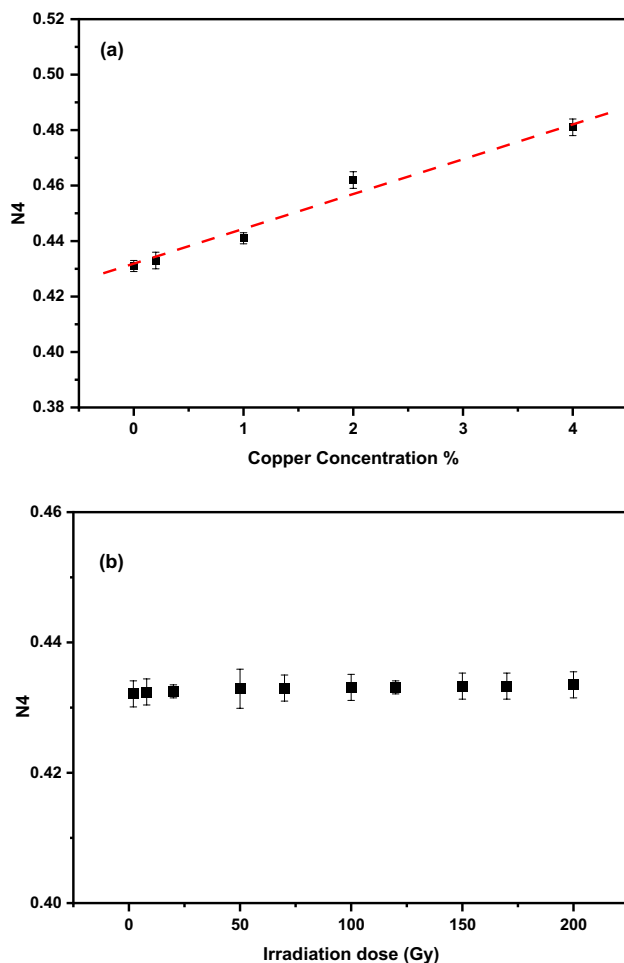


Fig. 25 a, b Variation of the four-coordinated boron as a function of copper oxide concentration and irradiation doses

[50]. Moreover, the modification in the borate matrix might also be explained by the existence of an alkali oxide, which enhanced the polymerization of the borate matrix [51]. Additionally, the coordination of boron changes from trigonal to tetrahedral. After that, some of the basic borate units would change from BO_3 into BO_4 groups.

3.4.3 DAT and Calculation of N_4 of the Selected Sample After Irradiation

To better understand the structural changes before and after irradiation, a deconvolution is performed (Figures 22, 23, 24) to resolve all smearing bands caused by overlapping of triangular and tetrahedral borate groups with symbols (BO_3 and BO_4), respectively. The percentage of N_4 coordination can be calculated from such data and used to interpret FTIR data concerning changes in bridging and non-bridging oxygen (BO and NBO).

Figure 25a and b show the variation in the N_4 coordination with varying Cu contents within the samples and the irradiation doses. It was clear that a change in the Cu content might cause a significant linear change in the four coordinated boron atoms (N_4) due to the variation in the number of non-bridging oxygens corresponding to the increasing Cu content. However, the irradiation process did not change the value of N_4 as they only indicated the formation of defects or the rearrangement of the structural units.

4 Conclusion

In this work, the gamma-ray-shielding capacity of prepared glasses was measured via gamma spectroscopy and the Phys-X/PSD software. We observed that the addition of CuO enhanced the shielding capacity; it increased $LAC/$ MAC and Z_{eff} by reducing the HVL, MFP, and EABF values. These results demonstrated that the BGCu-4.0 sample offered superior gamma-ray protection compared with the other samples.

Further, the Cu ions-doped bioactive borate glass exhibited 2.5 times that of alanine due to the new preparation method, which improved the dose estimation at the radiotherapy level. Further, we recommend the utilization of this new material as an ESR dosimeter. Different methods, such as the replacement of metal CuO, which allows the measurement of the gamma-radiation doses in the intermediate-dose range (2–200 Gy), was applied to enhance the sensitivity. In future works, we recommend using high linear energy transfer (high LET) radiation energy by doping modified glass with transition metals, especially in mixed radiation fields. The FTIR absorption spectra exhibited due to the distributions of the borate groups in triangular and tetrahedral BO_3 and BO_4 in their distinct wavenumber locations ($1200\text{--}1600\text{ cm}^{-1}$ and $800\text{--}1200\text{ cm}^{-1}$, respectively remarkable vibrational peaks within the midmost area ($400\text{--}1600\text{ cm}^{-1}$). The good dosimetric properties of such a modified material might make it a good candidate for the practical detection and monitoring of gamma-radiation doses.

Author contribution AMM: contributed in this study, Conceptualization, Methodology, Validation, Formal analysis, Investigation, Resources, Software, Data curation, Writing—original draft Writing—original draft, Writing—review & editing Writing. FMEE: contributed in this study, Methodology, Validation, Resources, Software, Project administration. AMA: contributed in this study, Resources, Software, Formal analysis, Writing—original draft, Data curation. HMD: contributed in this study, Validation, Formal analysis, Investigation, Resources, Writing—original draft Writing—original draft.

Funding Open access funding provided by The Science, Technology & Innovation Funding Authority (STDF) in cooperation with The Egyptian Knowledge Bank (EKB). This research did not receive any specific Grant from funding agencies in the public, commercial, or not for profit sectors.

Data availability The data and material were available.

Declarations

Conflict of interest There are no conflicts of interest about the present work that declare all relationships or interests of the manuscript's authors that could potentially influence or bias the submitted work.

Open Access This article is licensed under a Creative Commons Attribution 4.0 International License, which permits use, sharing, adaptation, distribution and reproduction in any medium or format, as long as you give appropriate credit to the original author(s) and the source, provide a link to the Creative Commons licence, and indicate if changes were made. The images or other third party material in this article are included in the article's Creative Commons licence, unless indicated otherwise in a credit line to the material. If material is not included in the article's Creative Commons licence and your intended use is not permitted by statutory regulation or exceeds the permitted use, you will need to obtain permission directly from the copyright holder. To view a copy of this licence, visit <http://creativecommons.org/licenses/by/4.0/>.

References

- W. Guo-hui, Man-li He, Fan-chao C, Jun-dong F and Yao-dong D. *Prog Nucl Energy* **112**, 225–232 (2019). <https://doi.org/10.1016/j.pnucene.2019.01.001>
- A.I. Elazaka, H.M.H. Zakaly, S.A.M. Issa, M. Rashad, H.O. Tekin, H.A. Saudi, V.H. Gillette, T.T. Erguzel, A.G. Mostafa, *J. Hazard. Mater.* **403**, 123738 (2021). <https://doi.org/10.1016/j.jhazmat.2020.123738>
- H.M. Diab, A.M. Abdelghany, H.S. Hafez, *J. Mater. Sci.* (2020). <https://doi.org/10.1007/s10854-020-04564-4>
- A.A. Abd-Elghany, H.M. Diab, A. Sulieman, *J. Radiat. Res. Appl. Sci.* **13**, 246–251 (2020). <https://doi.org/10.1080/16878507.2020.1727676>
- L.L. Hench, *J. Mater. Sci. Mater. Med.* **17**(11), 967–978 (2006). <https://doi.org/10.1007/s10856-006-0432-z>
- M. Marrale, L. Abbene, F. d'Errico, S. Gallo, A. Longo, S. Panzeca, L. Tana, L. Tranchina, F. Principato, *J. Radiat. Measur.* **106**, 1–5 (2017). <https://doi.org/10.1016/j.radmeas.2017.03.009>
- Y. Liu, L. Ma, J. Guo, G. Dong, J. Cong, Y. Ji, J. Ning, G. Yang, W. Ke, *PLoS ONE* **13**(5), e0197953 (2018). <https://doi.org/10.1371/journal.pone.0197953>
- S. Gallo, G. Iacoviello, A. Bartolotta, D. Dondi, S. Panzeca, M. Marrale, *Nucl. Inst. Methods Phys. Res. B* **407**, 110–117 (2017). <https://doi.org/10.1016/j.nimb.2017.06.004>
- A. Kinoshita, O. Baffa, S. Mascarenhas, *PLoS ONE* **13**(2), e0192444 (2018). <https://doi.org/10.1371/journal.pone.0192444>
- A. Romanyukha, F. Trompier, R.A. Reyes, *Radiat. Environ. Biophys.* (2013). <https://doi.org/10.1007/s00411-013-0511-8>
- M. Duval, *Radiat. Meas.* **79**, 24–32 (2015). <https://doi.org/10.1016/j.radmeas.2015.06.004>
- F.H. ElBatal, A.M. Abdelghany, H.A. ElBatal, *Spectrochim. Acta Part A Mol. Biomol. Spectrosc.* **122**, 461–468 (2014). <https://doi.org/10.1016/j.saa.2013.11.011>
- A.M. Abdelghany, Y.S. Rammah, *J. Inorg. Organomet. Polym. Mater.* **31**(6), 2560–2568 (2021). <https://doi.org/10.1007/s10904-020-01862-6>
- A. Hunyek, *J. King Mongkut's Univ. Technol. N. Bangk.* (2019). <https://doi.org/10.14416/j.kmutnb.2019.03.008>
- B.H. Rabee, N. Jabar, *J. Chem. Pharmaceut. Res.* **9**(5), 310–314 (2017)
- A.H. Almuqrin, M.I. Sayyed, *Appl. Sci.* **11**, 5697 (2021). <https://doi.org/10.3390/app11125697>
- P. Kaur, K.J. Singh, S. Thakur, P. Singh, B.S. Bajwa, *Spectrochim. Acta A* **206**, 367–377 (2019). <https://doi.org/10.1016/j.saa.2018.08.038>
- J. Singh, V. Kumar, Y.K. Vermani, M.S. Al-Buriah, J.S. Alzaharani, T. Singh, *Ceram Int* (2021). <https://doi.org/10.1016/j.ceramint.2021.04.188>
- K.S. Mann, *Nucl. Inst. Method. Phys. Res. A* **875**, 146–155 (2017). <https://doi.org/10.1016/j.nima.2017.09.001>
- E.M. Abou Hussein, A.M. Madbouly, F.M. EzzEldin, N.A. El Alaily, *J. Mater. Chem. Phys.* **261**, 124212 (2021). <https://doi.org/10.1016/j.matchemphys.2020.124212>
- O.I. Sallam, A.M. Madbouly, N.A. Elalaily, F.M. Ezz-Eldin, *J. Alloys Compds.* **843**, 156056 (2020). <https://doi.org/10.1016/j.jallcom.2020.156056>
- A.M. Madbouly, A. Alazab Huda, E. Borham, F.M. Ezz-ElDin, *J. Appl. Phys. A* **127**, 761 (2021). <https://doi.org/10.1007/s00339-021-04889-9>
- E.M. Abou Hussein, A.M. Madbouly, F.M. EzzEldin, *J. Mater. Sci.* **32**, 25933–25951 (2021). <https://doi.org/10.1007/s10854-021-05368-w>
- Y.S. Alajeramia, D. Drabold, M.H.A. Mhareb, K.L.A. Cimat, G. Chen, M. Kurudirek, *Ceram. Int.* **46**, 12718–12726 (2020). <https://doi.org/10.1016/j.ceramint.2020.02.039>
- M. Kurudirek, *J. Radiat. Environ. Biophys.* **53**, 175–185 (2014). <https://doi.org/10.1007/s00411-013-0502-9>
- M.I. Sayyed, H.C. Manjunatha, D.K. Gaikwad, S.S. Obaid, M.H.M. Zaid, K.A. Matori, *Dig. J. Nanomater. Bio.* **13**, 701–712 (2018)
- Y.S. Alajerami, D. Drabold, M.H.A. Mhareb, K. Leslee, A. Cimat, G. Chen, M. Kurudirek, *Ceram. Inter.* **46**, 12718–12726 (2020). <https://doi.org/10.1016/j.ceramint.2020.02.039>
- H.O. Tekin, S.A.M. Issa, E. Kavaz, E.E. AltunsoyGuclu, *J. Mater. Res. Exp.* **6**, 115212 (2019). <https://doi.org/10.1088/2053-1591/ab4cb5>
- B. Yasser Saddeek, A.M. Shams Issa, T. Alharbi, K. Aly, M. Ahmad, H.O. Tekin, *Ceram. Int.* **46**(3), 2661–2669 (2020). <https://doi.org/10.1016/j.ceramint.2019.09.254>
- H.O. Tekin, M.I. Sayyed, A.M. Issa Shams, *Radiat. Phys. Chem.* **150**, 95–100 (2018). <https://doi.org/10.1016/j.radphyschem.2018.05.002>
- K.A. Mahmoud, E. Lacomme, M.I. Sayyed, O.F. Ozpolat, O.L. Tashlykov, *J. Heliyon* **6**, e03560 (2020). <https://doi.org/10.1016/j.heliyon.2020.e03560>
- H.O. Tekin, T.T. Erguzel, M.I. Sayyed, V.P. Singh, T. Manici, E.E. Altunsoy, O. Agar, *Dig. J. Nanomater. Bio.* **13**, 381–389 (2018)
- L. Seenappa, H.C. Manjunatha, K.N. Sridhar, C. Hanumantharayappa, *Indian J. Pure Appl. Phys.* **56**, 383–391 (2018)
- A.M.A. Mostafa, S.A.M. Issa, H.M.H. Zakaly, M.H.M. Zaid, H.O. Tekin, K.A. Matori, H.A.A. Sidek, R. Elsaman, *Results Phys.* **19**, 103496 (2020). <https://doi.org/10.1016/j.rinp.2020.103496>
- A. El Abd, G. Mesbah, N.M.A. Mohammed, A. Ellithi, *J. Rad. Nucl. Appl.* **2**, 53–58 (2016)
- A.M. Abdelghany, H.A. ElBatal, F.M. EzzEldin, *Spectrochim. Acta A* **149**, 788–792 (2015). <https://doi.org/10.1016/j.saa.2015.04.105>
- J.C.L. Chow, *Handbook of Nanoparticles* (Springer International Publishing, Cham, 2016), pp. 41–65

38. S. Gallo, G. Iacoviello, A. Bartolotta, G. Iacoviello, A. Bartolotta, D. Dondi, S. Panzeca, M. Marrale, Nucl. Instr. Method. Phys. Res. Sect. B. (2017). <https://doi.org/10.1016/j.nimb.2017.06.004>
39. C. Gautam, A.K. Yadav, A.K. Singh, ISRN Ceram. (2012). <https://doi.org/10.5402/2012/428497>
40. F.H. Margha, A.M. Abdelghany, Process. Appl. Ceram. **6**(4), 183–192 (2012). <https://doi.org/10.2298/PAC1204183M>
41. S.H. Gordon, R.E. Harry-Okuru, A.A. Mohamed, Talanta **174**, 587–598 (2017). <https://doi.org/10.1016/j.talanta.2017.06.043>
42. C.M. Muller, B. Pejic, L. Esteban, C.D. Piane, M. Raven, B. Mizaikoff, Sci. Rep. **4**, 6764 (2014). <https://doi.org/10.1038/srep06764>
43. R. Bubnova, S. Volkov, B. Albert, S. Filatov, Curr. Comput. Aided Drug Des. **7**, 93 (2017). <https://doi.org/10.3390/cryst7030093>
44. A.M. Abdelghany, Spectrochim. Acta Part A Mol. Biomol. Spectrosc. **100**, 120–126 (2013). <https://doi.org/10.1016/j.saa.2012.02.051>
45. W.-B. Anja, M. Doris, P. Dimitrios, K. Efstratios, W. Lothar, J. Phys. Chem. B **119**(7), 3259–3272 (2015). <https://doi.org/10.1021/jp5120465>
46. H.O. Tekin, E. Kavaz, E.E. Altunsoy, O. Kilicoglu, O. Agar, T.T. Erguzel, M.I. Sayyed, Ceram. Int. **45**(8), 9934–9949 (2019). <https://doi.org/10.1016/j.ceramint.2019.02.036>
47. H.A. El Batal, E.M. Abou Hussein, N.A. El Daily, F.M. EzzEldin, J. Non-Cryst. Solids **528**, 119733 (2020). <https://doi.org/10.1016/j.jnoncrysol.2019.119733>
48. A. Okasha, A.M. Abdelghany, A.R. Wassel, A.A. Menazea, Radiat. Phys. Chem. **176**, 109018 (2020). <https://doi.org/10.1016/j.radphyschem.2020.109018>
49. F.H. ElBatal, S. Ibrahim, A.M. Abdelghany, J. Mol. Struct. **1030**, 107–112 (2012). <https://doi.org/10.1016/j.molstruc.2012.02.049>
50. A.A. Menazea, A.M. Abdelghany, Radiat. Phys. Chem. (2020). <https://doi.org/10.1016/j.radphyschem.2020.108932>
51. A.M. Abdelghany, A. Behairy, J. Mater. Res. Technol. **9**, 10491–10497 (2020). <https://doi.org/10.1016/j.jmrt.2020.07.057>

Publisher's Note Springer Nature remains neutral with regard to jurisdictional claims in published maps and institutional affiliations.